Supplemental Data

The Influence of Cell Mechanics, Cell-Cell Interactions, and Proliferation on Epithelial Packing

Reza Farhadifar, Jens-Christian Röper, Benoit Aigouy, Suzanne Eaton, and Frank Jülicher

Supplemental Results

Displacement of Vertices in the Epithelial Field after Laser Ablation

To quantify the displacement of vertices in the field of cells surrounding the cut site, we used a polar coordinate system in which r denotes the radial distance from the cut point and ϑ denotes the angle with respect to the orientation of the cut boundary. The angle of the cut boundary thus corresponds to $\vartheta = 0$ and π. For each vertex, we determined the radial and tangential components D_r and D_ϑ of the displacement vectors D (Figure S6A). The radial displacements D_r depend on the angle ϑ relative to the orientation of the cut boundary (Figure S6C). They are maximal for vertices lying along the cut-bond axis. The radial displacements D_r of those vertices lying in a direction perpendicular to the cut boundary (i.e., near $\vartheta = \pi/2$ or $3\pi/2$) were small and did not exceed background noise. Radial displacements decreased quickly for increasing distance r from the cut bond. At distances beyond six average edge lengths, they only marginally exceeded the background noise (compare the top and bottom panels in Figure S6C). Tangential displacements D_ϑ were smaller and decreased more quickly with increasing distance from the cut site (Figure S7A).

To test whether the vertex model can account for displacements in the larger field around the removed bond, we simulated laser ablation with parameter values corresponding to case I (see Figure 1), calculated radial displacements of vertices at different distances from the bond with respect to the polar angle ϑ, and compared them to observed displacements. Like the area and perimeter changes, the radial and tangential displacements of vertices D_r and D_ϑ in the surrounding network were quantitatively reproduced by our simulations (compare Figures S6C and S6D; Figures S7A and S7B). As in the experimental data, maxima of D_r occur at angles 0 and π, whereas maxima of D_ϑ occur at $3\pi/4$ and $7\pi/4$ (Figures S6D and S7B). For radial displacements, the magnitude of maximal average displacements, as well as their scatter, agreed quantitatively with those found in experiments and decreased by similar amounts over similar distances. For tangential displacements, agreement was also good—however, note that for small r, the average of the amplitudes differs by a factor of two. More data points would be necessary for determining whether this difference is significant or not.

Simulating Cell-Shape Changes after Laser Ablation

We could not say a priori whether laser ablation affected only localized line tension of cell boundaries (scenario I; Figure S8A) or whether perimeter contractility was affect as well (scenario II, Figure S8B). To investigate this, we simulated laser ablation by using both scenarios and tested which best fit the deformations occurring in experiments. For simulations of laser ablation, agreement between theory and experiment requires that we remove both the line tension and contractility of the two adjacent cells; if we keep $\overline{\Gamma}_\alpha = \overline{\Gamma}$ for the cells adjacent to the cut (scenario I in Figure S8A), calculated movements are very different from the observed ones (compare Figures S8C and S8D to Figures S8E and S8F).

An Annealing Model for Hexagonal Repacking

The observation that packing geometry in the larval disc reflects a local minimum suggests that the system could convert to a more hexagonal array by mechanisms in which fluctuations induce rearrangements, which are then biased by the energy function toward the hexagonal ground state. This is analogous to annealing, during which crystalline order is approached in a physical context [S1, S2]. During hexagonal repacking, the endocytosis and recycling of cadherin increases, and cell-boundary lengths fluctuate [S3]. Boundary fluctuations, driven by changes in cell-boundary tension, might allow wing epithelial cells to explore different packing configurations and thus move the system toward the hexagonal ground state. To demonstrate the feasibility of this idea, we performed simulations by starting with an irregularly packed network configuration in which proliferation had ceased and introduced stochastic changes of line tensions $\overline{\Lambda}_{ij}$ at randomly chosen cell boundaries (see Experimental Procedures). After each stochastic variation, the system was relaxed to the nearest stable state. As this process is repeated, the network morphology attains a new stationary state with a characteristic distribution of polygon classes. The system can be annealed by slow reduction of the strength of fluctuations. An example of such an annealing process is shown in Movie S6 and indeed leads to increased hexagonal order, similar to that of the pupal wing. Thus, we might be able to achieve hexagonal repacking by controlling
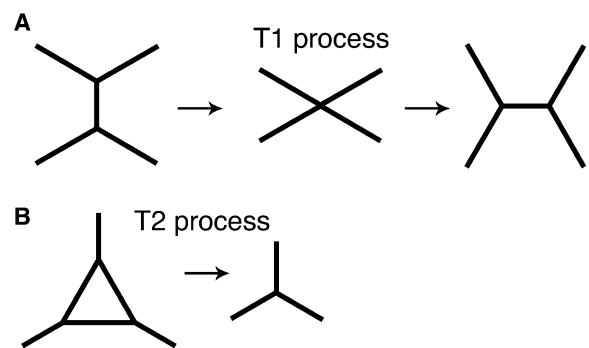

Figure S1. T1 and T2 Processes

(A) T1 process. The bond length between two three-way vertices first shrinks to zero and subsequently expands in the opposite direction. This causes local changes in neighbor numbers of surrounding cells.
(B) T2 process. If the area of a triangle shrinks to zero, it is replaced by a vertex. This corresponds to extrusion of a cell from the epithelium.
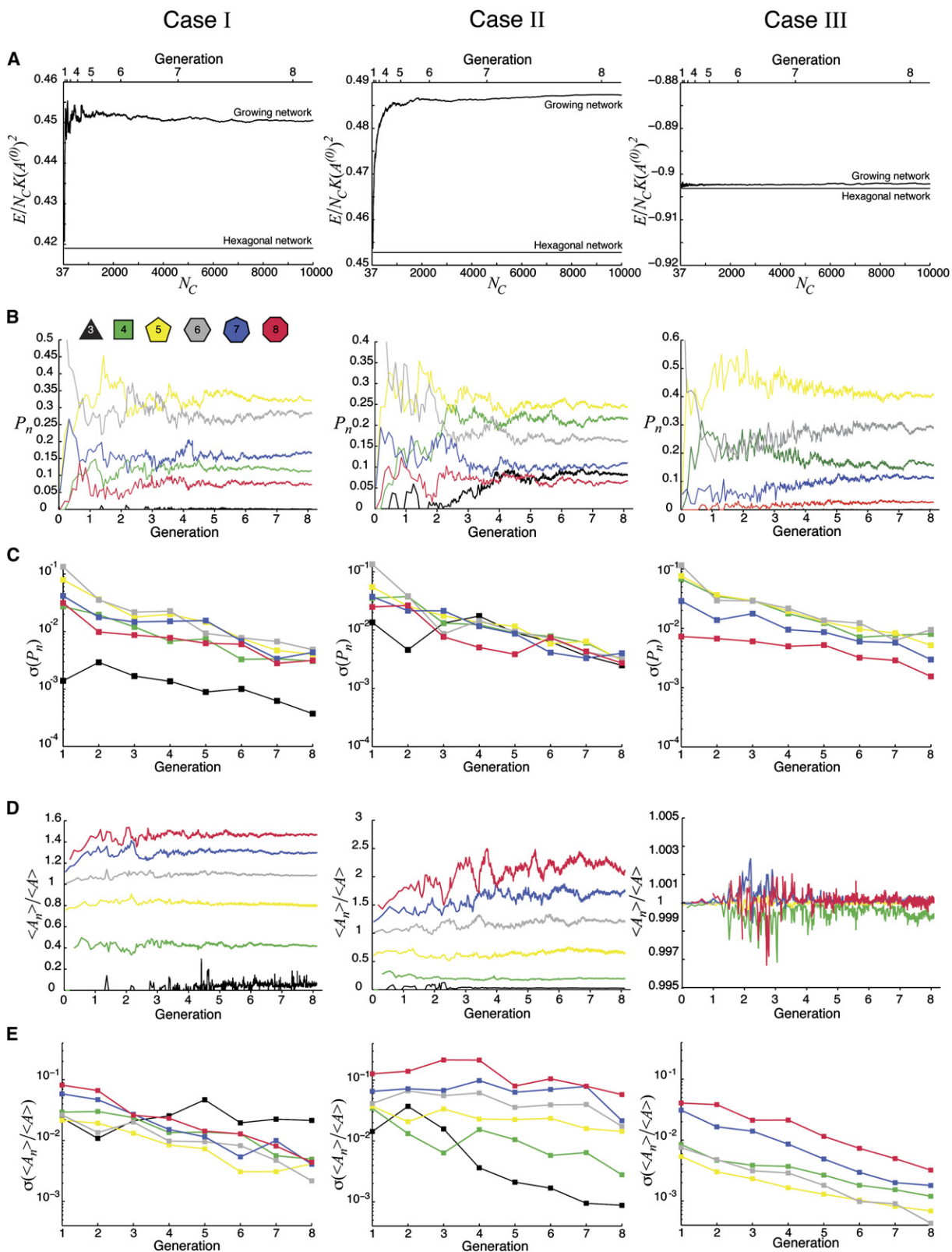
Figure S2. Properties of Networks Generated by Repeated Cell Division

(A) Energy per cell normalized by the reference elastic energy $K(A^{(0)})^2$ as a function of cell number N_C in simulations of network growth for the three cases I, II, and III indicated in Figure 1. The generation number is also indicated. The energy of the corresponding hexagonal network is indicated. In case III, the small energy difference between ground state and simulation is due to numerical errors.

(B) Distribution P_n of neighbor numbers as a function of generation number for the same cases.
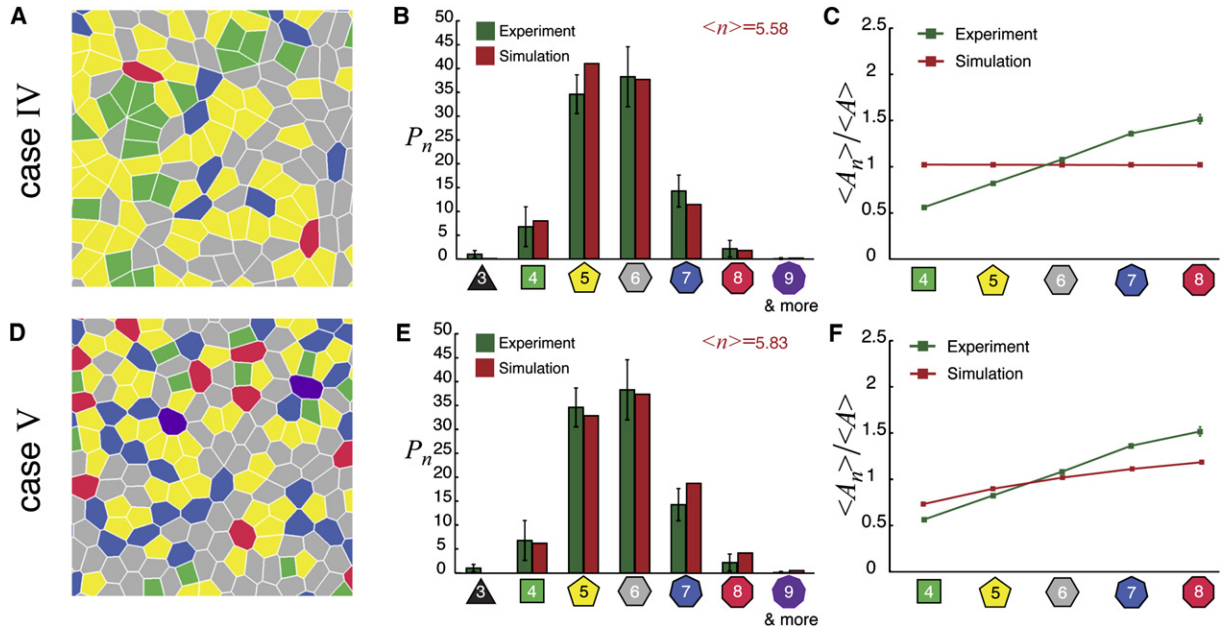
Figure S3. Packing Geometry in Simulations of Case IV and V

(A–C) Network morphology (A), polygon class distribution ([B], red bars), and area variation ([C], red line) generated by repeated cell division in case IV. Green bars in (B) and the green line in (C) indicate experimental values for the third instar wing epithelium.
(D–F) Similar plots for case V.

the strength of fluctuations in adhesion or contractility at individual cell boundaries.

Supplemental Experimental Procedures

Simulations and Data Analysis

In our simulations of the vertex model, we use periodic boundary conditions and relax the energy function given in Box 1 by using a conjugate gradient method (see [S4]). In this procedure, the size of the simulation box is also relaxed. During energy minimization, the network connectivity is changed according to T1 transitions if two vertices approach each other, and such a transition leads to further energy minimization. Similarly, if a triangular cell area approaches zero, the three vertices of this cells are identified, thereby leading to removal of this cell by a T2 transition. During simulations of proliferation, the network is relaxed until the relative energy change between relaxation steps drops below 10^{-8}. In our simulations of annealing toward a hexagonal lattice, we randomly vary $\Lambda_{ij} = \Lambda(1 \pm \mu)$ at randomly selected bonds $\langle i, j \rangle$, for which μ is the noise strength and $\langle \Lambda_{ij} \rangle = \Lambda$ is unchanged.

We quantify the differences between theoretical and experimental results by the quantities Δ_P, Δ_A, and Δ_L. The difference between the experimentally observed neighbor number distribution $P_n^{\exp}$ and the one obtained by simulations P_n^{sim} is measured by $\Delta_P = \sum_{n=3}^{\infty} (P_n^{sim} - P_n^{\exp})^2$. The red region in Figure 3 indicates those parameter values for which $\Delta_P < 0.004 \approx 0.1(\Delta_{\max} - \Delta_{\min})$ for which $\Delta_{\min}$ and $\Delta_{\max}$ denote the minimal and maximal values of Δ_P found in our simulations.

Similarly, the difference between experimentally determined average areas of n sided cells $\langle A_n^{\exp} \rangle$ and those obtained in our simulations $\langle A_n^{sim} \rangle$ were quantified by $\Delta_A = \sum_n (\langle A_n^{sim} \rangle / \langle A^{sim} \rangle - \langle A_n^{\exp} \rangle / \langle A^{\exp} \rangle)^2$. The blue region in Figure 3 corresponds to $\Delta_A < 0.07$.

To compare simulation and experiment for laser ablation, we fit a straight line to the determined variation of normalized area change ΔA_{cut} as a function of normalized bond-length increase $\Delta \ell$ (Figures

5C and 5E). We quantify the difference that is between experiment and simulation by Δ_L; it is the absolute difference between the slopes of the fit. The green region in Figure 3 corresponds to $\Delta_L < 0.07$ with the additional constraint that average perimeter change is > 0.

Fly Strains

Flies ubiquitously expressing E-cadherin under the control of the ubiquitin promoter [S5] were used for morphology analysis and laser-ablation experiments.

Mysosin regulatory light chain (RLC) was visualized with *sqhAX3*; P [*w, sqh-GFP42*], in which sqh-GFP42 is the only source of myosin II RLC [S6].

Imaging

Third instar wing imaginal discs of *Drosophila melanogaster* were dissected and mounted for live imaging in Schneiders Insect Media (Sigma) with or without FM 4-64 10 μg/ml (Molecular Probes). We used double-sided tape as a spacer to build a small flow chamber between a glass slide and coverslip in order to prevent squeezing of the sample.

Fluorescence images of E-cadherin and phalloidin-stained actin were taken from fixed samples of ubiquitously E-cadherin-GFP-expressing flies. Wing discs were dissected in PBS and fixed with 4% formaldehyde in PBS for 20 min. After being rinsed three times in PBS containing 0.3% Triton X-100, wing discs were incubated with 1 μM Rhodamin-phalloidin (Molecular Probes) at room temperature for 2 hr. Then, they were rinsed three times in PBS (15 min each wash) and mounted in antibleach medium (Vectashield). Third instar imaginal discs were fixed and stained as described [S7] so that both dividing and apoptotic cells could be detected. Dividing cells were detected with anti-phospho-histone H3 (Ser10, 1:1000). Apoptotic cells were detected with anti-cleaved Caspase-3 (Asp 175, 1:200). Both antibodies were obtained from Cell Signaling Technology.

(C) Standard deviation $\sigma(P_n)$ of the neighbor number distribution as a function of generation number $log_2(N_C/N_0)$ for which $N_0 = 36$ is the initial cell number.
(D) Average area of n sided cells $\langle A_n \rangle$ relative to the average area $\langle A \rangle$ of all cells as a function of generation number.
(E) Standard deviation $\sigma(\langle A_n \rangle / \langle A \rangle)$ of the relative average area of n sided cells as a function of generation number.

Table S1. Polygon Class Distributions

	P_3	P_4	P_5	P_6	P_7	P_8	P_9 and More	$\langle n \rangle$
Drosophila wing disc	1.00 ± 0.77	6.78 ± 4.176	34.61 ± 4.06	38.28 ± 6.29	14.28 ± 3.36	2.17 ± 1.76	0.06 ± 0.24	5.51
Case I	0.11	11.29	32.10	28.39	16.79	7.31	4.02	5.90
Case II	8.21	21.63	24.39	16.18	10.92	6.63	12.05	5.95
Case III	0.05	15.73	40.62	29.20	11.25	2.70	0.45	5.46
Case IV	0.02	7.95	41.07	37.72	11.41	1.71	0.12	5.58
Case V	0.02	6.24	32.86	37.32	18.76	4.23	0.57	5.83

Immunofluorescence images were taken with a Leica TCS SP2 confocal laser-scanning microscope equipped with a PL-Apochromat 63× NA 1.32 objective and 8× zoom. All others images were taken with the spinning-disc microscope described below.

Figures were prepared with Photoshop and Illustrator (Adobe).

Laser-Ablation Experiments

Laser-ablation experiments in third instar wing imaginal discs were performed with a pulsed, third-harmonic, solid-state UV laser (λ = 355 nm, 400 ps, 20 μJ/pulse, PowerChip, JDS Uniphase). The laser beam was focused to a fixed spot of approximately 1.3 μm in the focal plane. In the z direction, the focus is only slightly more extended. By comparison, the length of disc epithelial cells in the z direction is greater than 30 μm. The laser focus is aimed at adherens junctions and ablates a small volume element at the junctions. We used an inverted microscope (Axiovert 200 M, Zeiss) equipped with a water-immersion lens (C-Apochromat 63× NA 1.2, Zeiss), a high-speed spinning-disc confocal system (CSU10, Yokogawa), and a cooled B/W CCD digital camera (ORCA-ER, Hamamatsu). A Melles Griot ArIon Laser (λ = 488 nm, 100 mW) was used for excitation of enhanced green fluorescent protein and FM4-64 (Molecular Probes).

The CCC software (Alfons Riedinger, Nick Salmon, and Ernst H. K. Stelzer, EMBL) controlled the laser and the microscope. A total of 30 laser pulses at 100 Hz were applied to the middle of a boundary. Images were taken every 5 s over a period of several minutes.
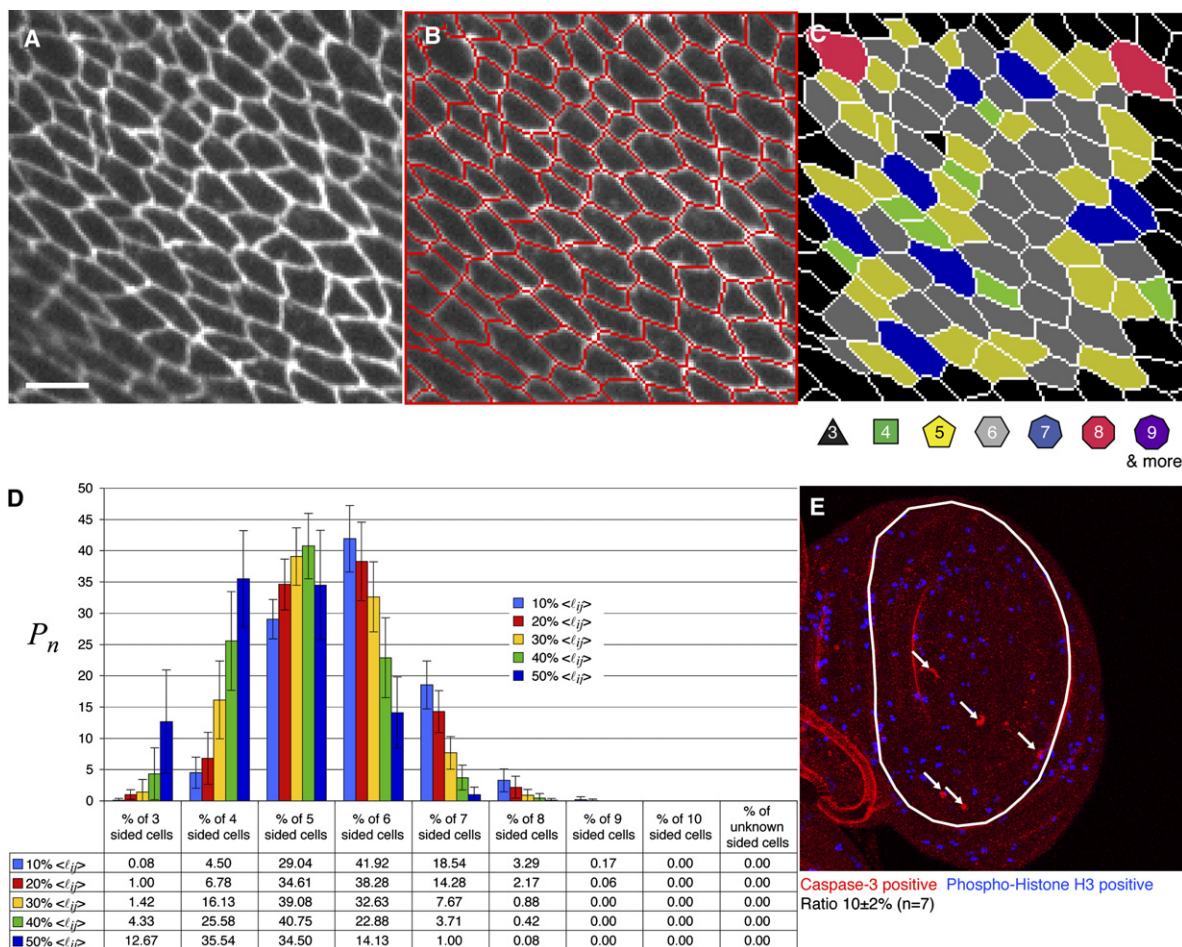

								% of
	% of 3 sided cells	% of 4 sided cells	% of 5 sided cells	% of 6 sided cells	% of 7 sided cells	% of 8 sided cells	% of 9 sided cells	% of 10 sided cells	% of unknown sided cells
10% $<\ell_{ij}>$	0.08	4.50	29.04	41.92	18.54	3.29	0.17	0.00	0.00
20% $<\ell_{ij}>$	1.00	6.78	34.61	38.28	14.28	2.17	0.06	0.00	0.00
30% $<\ell_{ij}>$	1.42	16.13	39.08	32.63	7.67	0.88	0.00	0.00	0.00
40% $<\ell_{ij}>$	4.33	25.58	40.75	22.88	3.71	0.42	0.00	0.00	0.00
50% $<\ell_{ij}>$	12.67	35.54	34.50	14.13	1.00	0.08	0.00	0.00	0.00

Caspase-3 positive Phospho-Histone H3 positive
Ratio 10±2% (n=7)

Figure S4. Packing Analyzer Output and Rate of Cell Elimination In Vivo

(A–C) The original image of a cadherin-stained wing (A) next to the corresponding outputs of the Packing analyzer program. (B) shows the network of boundaries and vertices generated by Packing analyzer, and (C) shows polygon class assignment.

(D) Colored bars indicate the fraction of cells assigned to different polygon classes when a vertex is defined as a cell contact that is less than 10% (light blue), 20% (red), 30% (yellow), 40% (green), or 50% (dark blue) of the average cell-boundary length.

(E) A third instar wing disc stained with antibodies to phopho-histone H3 (blue) and cleaved-Caspase (red). Anti-phospho-histone H3 stains cells in mitosis and anti-cleaved-Caspase stains cells in apoptosis (arrows) are shown. The wing pouch is outlined by a white circle. Average counts of cells positive for each in seven different discs are indicated.

Table S2. Area Variation

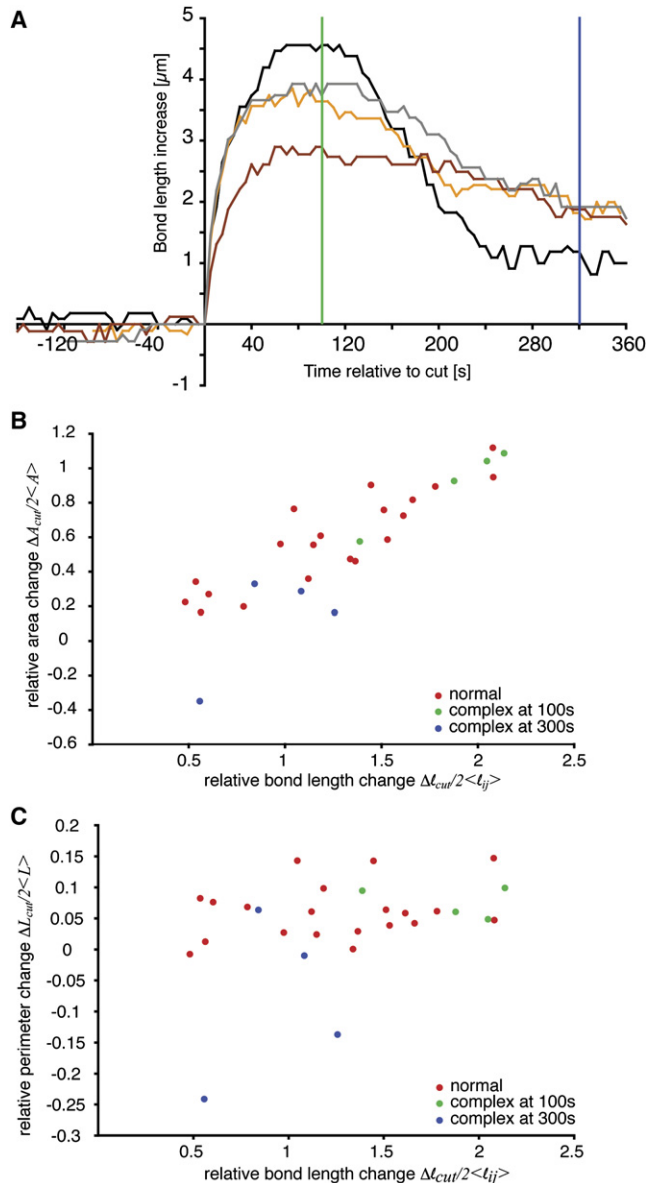|	$\langle A_3 \rangle / \langle A \rangle$	$\langle A_4 \rangle / \langle A \rangle$	$\langle A_5 \rangle / \langle A \rangle$	$\langle A_6 \rangle / \langle A \rangle$	$\langle A_7 \rangle / \langle A \rangle$	$\langle A_8 \rangle / \langle A \rangle$
Drosophila wing disc	0.42 ± 0.144	0.56 ± 0.02	0.82 ± 0.01	1.08 ± 0.01	1.36 ± 0.02	1.52 ± 0.05
Case I	0.05	0.42	0.80	1.08	1.30	1.47
Case II	0.03	0.20	0.65	1.21	1.73	2.06
Case III	1.0	1.0	1.0	1.0	1.0	1.0
Case IV	1.0	1.0	1.0	1.0	1.0	1.0
Case V	0.36	0.74	0.91	1.03	1.19	1.26

Figure S5. Complex Movements after Laser Ablation

(A) Bond-length increase as a function of time for four (out of 24) cases in which more complex movements were observed upon laser ablation. The distance between vertices at either end of the ablated bond $d - d_0$ increased initially and reached a maximum at approximately 90 s after cut, after which the distance decreased again. After 360 s, the distance was still greater than the initial distance before the cut.

(B and C) Relative area (B) and perimeter (C) changes as a function of relative bond-length increase were plotted at the time corresponding to maximum vertex displacement (green dots) and at the time at which vertices have moved closer together (blue dots). Values corresponding to maximum vertex displacement (green dots) are most consistent with the other 20/24 experiments (red dots). Thus, the maximal displacements probably reflect immediate mechanical relaxation in response to ablation. Subsequent movements reversing the initial bond-length increase might then reflect active cellular processes aimed at reconstructing the junction. These might occur when the laser pulse does not completely destroy the ability of cells to reconstruct their boundary.

Drug Treatment

Wing imaginal discs were incubated after dissection for 40 min in Schneiders medium containing Y-27632 dihydrochloride monohydrate (250 μM) from Sigma for Rho-Kinase (ROCK) inhibition before laser ablation.

Automated Image Analysis

Images were analyzed with "packing analyzer" software developed by us. This software segments confocal images and detects cell outlines with the watershed algorithm [S8]. Oversegmentation and undersegmentation is corrected automatically, on the basis of pixel

Table S3. Rate of T1 and T2 Transitions

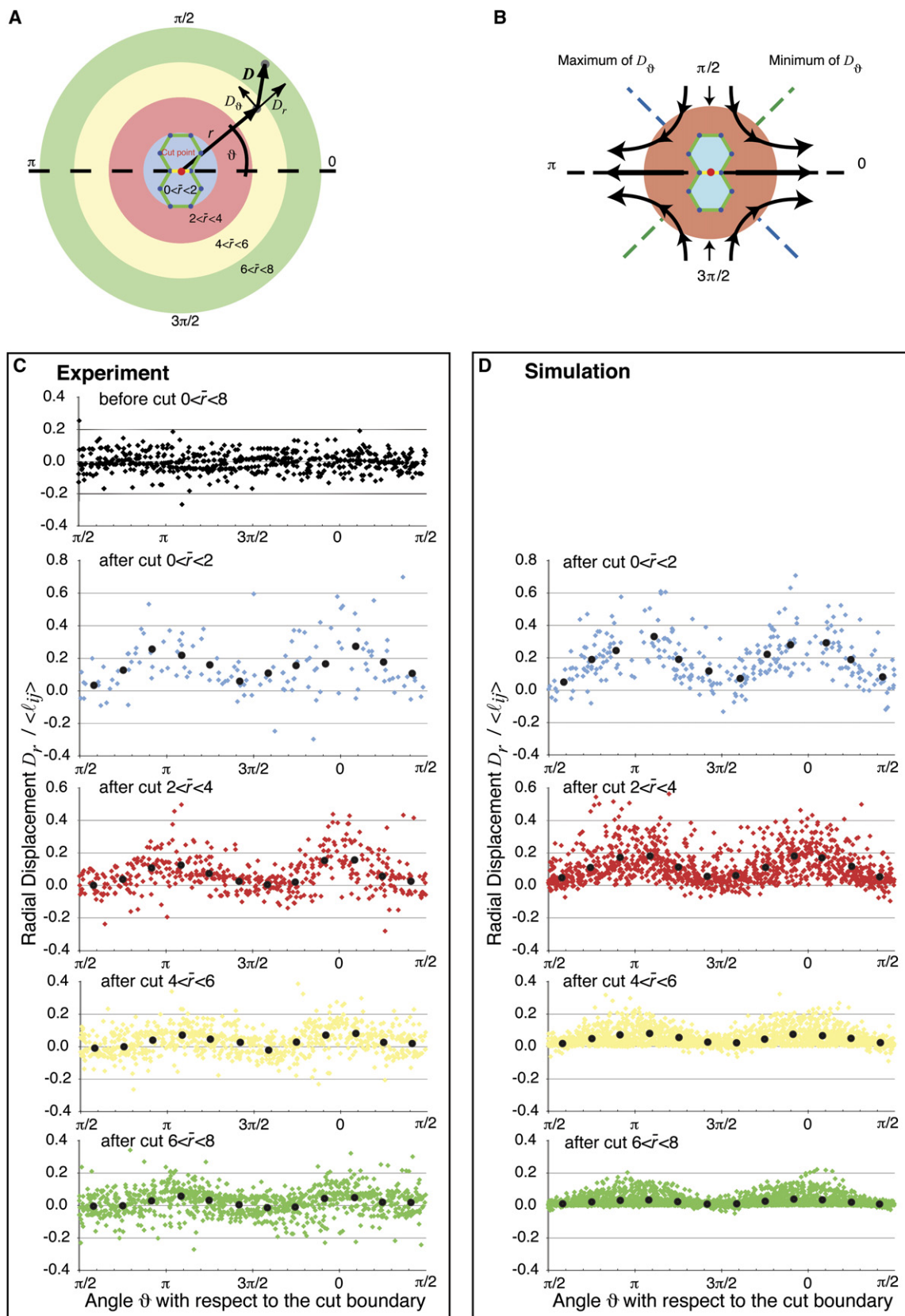|	T1 Transitions per 100 Divisions	T2 Transitions per 100 Divisions
Case I	37	12
Case II	16	3
Case III	146	0
Case IV	162	0
Case V	74	0

Figure S6. Vertex Displacement Fields: Radial Displacements

(A) Schematic representation of positions and displacements during a laser ablation experiment. The direction of the cut boundary is indicated by a dashed black line. The position of a vertex before ablation is described by its radial distance r from the cut point and its angle ϑ with respect
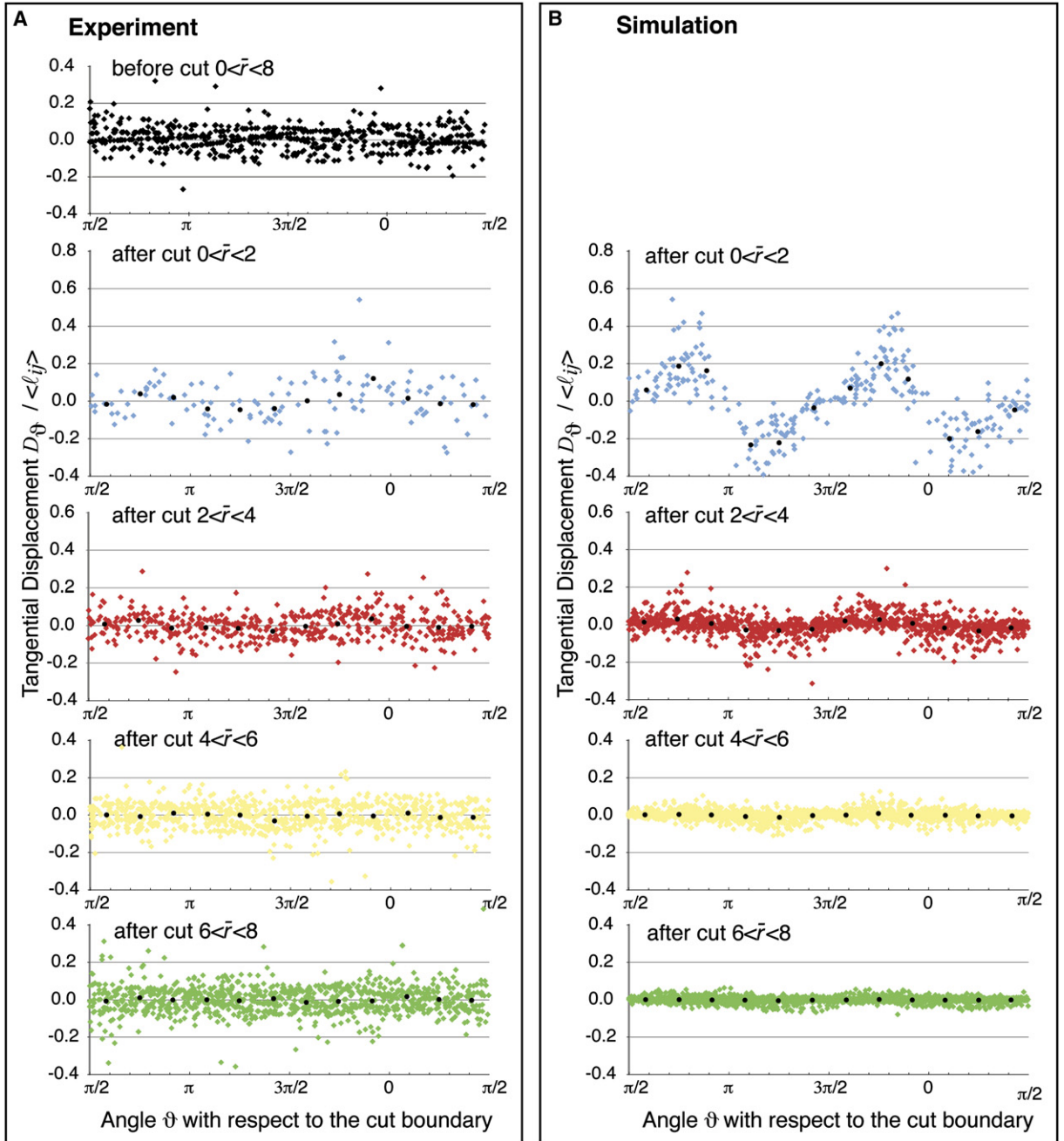
Figure S7. Vertex Displacement Fields: Tangential Displacements

(A and B) Tangential displacements D_ϑ of vertices relative to the average bond length $\langle \ell_{ij} \rangle$ as a function of the angle ϑ indicated in Figure S6A. Vertices at different distances from the ablation point are shown in the colors used in Figure S6. Black dots show the average displacement for vertices at different angles, grouped in bins of $\pi/6$ radians. (A) shows tangential displacements observed in 20 different experiments. (B) shows tangential displacements obtained in the 50 simulations of bond removal, for which the radial displacements are shown in Figure S6D. The first panel in (B) illustrates the tangential displacement before laser ablation.

to the cut-bond orientation. The movement of the vertex from its initial position to its new position after the cut is described by its displacement vector $\boldsymbol{D}$. This vector can be decomposed in radial and tangential components D_r and D_ϑ. Vertices are grouped in concentric rings according to their normalized distance from the cut point $\bar{r} = r / \langle \ell_{ij} \rangle$ relative to the average bond length $\langle \ell_{ij} \rangle$.

(B) Schematic representation of the displacements after the ablation of a bond. Along the bond direction, displacements are outward. Perpendicular to the bond, displacements are smaller and inward. This leads to the anisotropic displacements shown.

(C) Radial displacements D_r of vertices normalized to the average bond length $\langle \ell_{ij} \rangle$ observed in 20 laser ablation experiments shown as a function of ϑ. The colors correspond to the distance ranges shown in (A). Black dots show the average displacements determined by grouping vertices in bins of $\pi/6$ radians.

(D) Normalized radial displacements obtained in 50 simulations of bond ablation with a network corresponding to case I. In these simulations, $\overline{\Lambda}_{ij} = 0$ for the single bond that is removed, and $\overline{\Gamma}_\alpha = 0$ for the two adjacent cells.
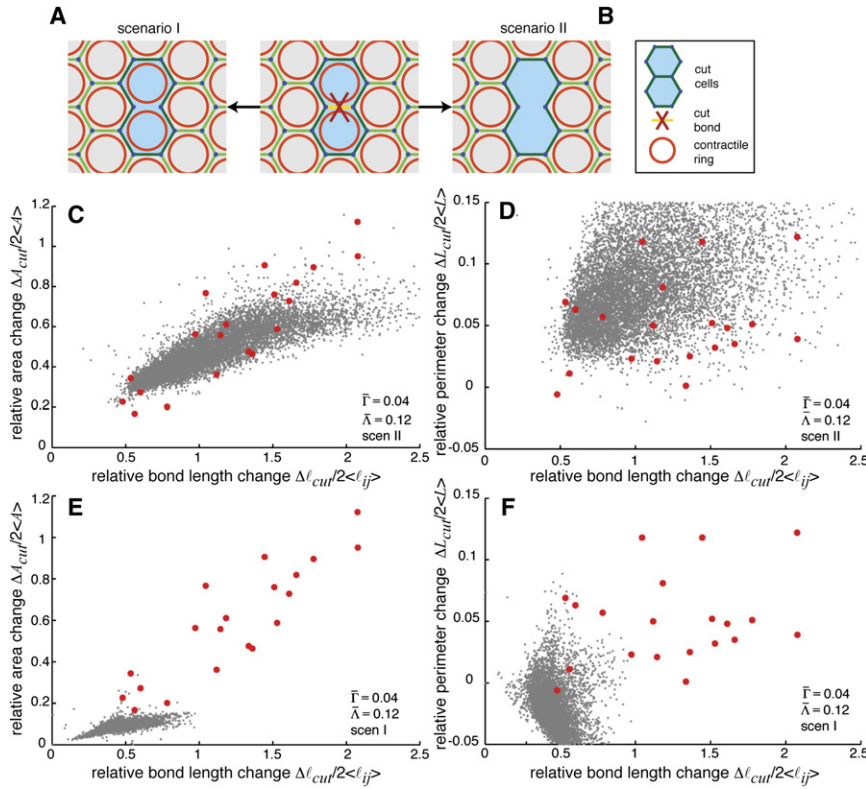
Figure S8. Different Methods for Simulating Laser Ablation

(A and B) In scenario I, ablation is simulated by setting only $\Lambda_{ij} = 0$ for the cut bond. In scenario II, ablation is simulated by setting both $\Lambda_{ij} = 0$ and $\Gamma_\alpha = 0$ for the two cells adjacent to the cut boundary.

(C and D) Comparison of relative area (C) and relative perimeter (D) changes as a function of relative bond-length increase when laser ablation is simulated with scenario II. Parameter values for surrounding cells are indicated.

(E and F) Comparison of relative area (E) and relative perimeter (F) changes as a function of relative bond-length increase when laser ablation is simulated with scenario I and the same parameter values as in (C) and (D).

intensity, and manually for removal of remaining mistakes. The software identifies three- and four-way vertices on the basis of their shape by using a 3 × 3 pixel box to scan the watershed mask. Finally, the software determines the polygon class of each cell by counting its number of vertices; this number is corrected in order so that boundaries less than 2 pixels in length (20% of average cell-boundary length) could be excluded. Boundaries shorter than this are identified as a four-way vertex, and the polygon class of the cell is corrected accordingly. The software automatically calculates the individual bond length and the area and perimeter of each cell. Further data analysis was done with Excel, Matlab, and ImageJ. For the area variability plots, areas of individual cells were normalized to the average area within that wing disc.

Area and Perimeter Changes

Vertices at either end of the cut bond were tracked manually with ImageJ. We calculated the increase in distance between the vertices at either end of the ablated bond $d - d_o$ as a function of time by subtracting the initial distance d_o between the vertices from the actual distance $d_o + d$ at a particular time point. In order to determine the final distance $d_0 + d_1$ and the relaxation time τ, we fitted a single exponential function to the curve by using Matlab.

The combined area A_{cut} of the two cells sharing the cut bond as well as their combined perimeter L_{cut} was determined before the cut and at two times τ. The combined perimeter corresponds to the perimeter of the two cells sharing the cut bond without counting the cut bond itself.

The combined area was normalized to twice the average area of cells in the image $\Delta A_{cut}/2<A>$ so that we could account for overall differences in size due to feeding conditions, for example. The combined perimeter was normalized to twice the average perimeter

$\Delta L_{cut}/2<L>$. The cut-bond length was normalized to the average bond length within a disc.

Displacement Field

Vertex positions before the cut were translated into a polar coordinate system, taking the cut point as origin and the angle ϑ with respect to the cut-bond orientation. Vertex movements were calculated as displacements vectors D originating from the initial vertex position before the cut and ending at the vertex position after 60 s. We corrected displacements for overall movements by subtracting the average movement of all vertices in the field. These displacement vectors were then separated into their radial and tangential components, D_r and D_ϑ respectively, with $D_r = \cos\vartheta \cdot D^x + \sin\vartheta \cdot D^y$ and $D_\vartheta = -\sin\vartheta \cdot D^x + \cos\vartheta \cdot D^y$ for which D^x denotes the component of D lying along the x axis and D^y the component along the y axis. We choose the x axis along the cut bond and the y axis perpendicular to it.

In order to determine background movements of vertices, we calculated displacement vectors over 60 s before the cut in the same way. The later cut point was used as the coordinate origin. For both simulations and experiments, we restricted our analysis to bonds at least the average bond length. Smaller bonds could not be accurately ablated in the wing disc without affecting adjacent cells.

Supplemental References

S1. Hamacher, K., and Wenzel, W. (1999). The scaling behaviour of stochastic minimization algorithms. Phys. Rev. E Stat. Phys. Plasmas Fluids Relat. Interdiscip. Topics *59*, 938–941.

S2. Kirkpatrick, S., Gelatt, C.D., and Vecchi, M.P. (1983). Optimization by simulated annealing. Science *220*, 671–680.

S3. Classen, A., Anderson, K., Marois, E., and Eaton, S. (2005). Hexagonal packing of *Drosophila* wing epithelial cells by the planar cell polarity pathway. Dev. Cell *9*, 805–817.

S4. Press, W.H., Teukolsky, S.A., Vetterling, W.T., and Flannery, B.P. (1992). Numerical Recipes in C: the Art of Scientific Computing, Second Edition (Cambridge: Cambridge University Press).

S5. Oda, H., and Tsukita, S. (1999). Dynamic features of adherens junctions during Drosophila embryonic epithelial morphogenesis revealed by a Dalpha-catenin-GFP fusion protein. Dev. Genes Evol. *209*, 218–225.

S6. Royou, A., Sullivan, W., and Karess, R. (2002). Cortical recruitment of nonmuscle myosin II in early syncytial Drosophila embryos: Its role in nuclear axial expansion and its regulation by Cdc2 activity. J. Cell Biol. *158*, 127–137.

S7. Greco, V., Hannus, M., and Eaton, S. (2001). Argosomes: A potential vehicle for the spread of morphogens through epithelia. Cell *106*, 633–645.

S8. Vincent, L., and Soille, P. (1991). Watersheds in digital spaces: An efficient algorithm based on immersion simulations. IEEE Trans. Pattern Anal. Mach. Intell. *13*, 583–598.